

Multi-resolution super learner for voxel-wise classification of prostate cancer using multi-parametric MRI

Jin Jin^a, Lin Zhang^b, Ethan Leng^c, Gregory J. Metzger^d, Joseph S. Koopmeiners^b

^aDepartment of Biostatistics, Bloomberg School of Public Health, Johns Hopkins University, Baltimore, MD, USA; ^bDevision of Biostatistics, School of Public Health, University of Minnesota, Minneapolis, MN, USA; ^cDepartment of Biomedical Engineering, University of Minnesota, Minneapolis, MN, USA; ^dDepartment of Radiology, University of Minnesota, Minneapolis, MN, USA.

ARTICLE HISTORY

Compiled May 28, 2022

ABSTRACT

While current research has shown the importance of Multi-parametric MRI (mpMRI) in diagnosing prostate cancer (PCa), further investigation is needed for how to incorporate the specific structures of the mpMRI data, such as the regional heterogeneity and between-voxel correlation within a subject. This paper proposes a machine learning-based method for improved voxel-wise PCa classification by taking into account the unique structures of the data. We propose a multi-resolution modeling approach to account for regional heterogeneity, where base learners trained locally at multiple resolutions are combined using the super learner, and account for between-voxel correlation by efficient spatial Gaussian kernel smoothing. The method is flexible in that the super learner framework allows implementation of any classifier as the base learner, and can be easily extended to classifying cancer into more sub-categories. We describe detailed classification algorithm for the binary PCa status, as well as the ordinal clinical significance of PCa for which a weighted likelihood approach is implemented to enhance the detection of the less prevalent cancer categories. We illustrate the advantages of the proposed approach over conventional modeling and machine learning approaches through simulations and application to in vivo data.

KEYWORDS

Multi-parametric MRI; multi-resolution modeling; ordinal clinical significance of PCa; super learner; voxel-wise classification

1. Introduction

Prostate cancer (PCa) is the second most common cancer and the second leading cause of cancer death among men in the U.S. According to the American Cancer Society, approximately 1 in 9 men will be diagnosed with PCa during his lifetime, and there is an expectation of 191930 new cases with 33330 deaths from PCa in 2020 in the United States [2]. In recent years, Multi-parametric magnetic resonance imaging (mpMRI) has become an increasingly important tool for evaluating the extent of PCa and determining the corresponding treatment strategy, such as needle biopsy or focal therapy [6, 12]. Traditionally, mpMRI examinations are used to manually delineate the cancerous re-

CONTACT Jin Jin. Email: jjin31@jhu.edu. Department of Biostatistics, Bloomberg School of Public Health, Johns Hopkins University, Baltimore, MD 21205, USA

gions within the prostate, which requires high efficiency due to time constraints and depends highly on radiologists' and urologists' expertise. Such methods have been criticized for the large variability in radiological assessment and human error [10], which motivated the development of automatic, quantitative predictive methods that address the limitations of direct radiological interpretation [18]. For voxel-wise classification of PCa, most current research focuses on the binary status of PCa, i.e. cancer or not cancer. Representative methods include regression-based models, clustering methods, kernel methods, naive Bayes, neural network, graphical models, and other commonly implemented machine learning-based approaches [3, 19–21, 23, 24, 27–30, 32]. Textural feature models have also been developed [9, 17].

Prior research revealed important structures in the mpMRI data, including regional heterogeneity, i.e. the heterogeneity in the distribution of both the predictors (the observed mpMRI parameters) and the outcome (the voxel-wise cancer status) both between and within the two main zones of the prostate, the central gland (CG) and the peripheral zone (PZ), as well as between-voxel correlation within each prostate. These have rarely been thoroughly investigated for voxel-wise PCa classification [15, 16, 25]. Recently, systematic modeling of the mpMRI structures under a Bayesian hierarchical modeling framework was discussed, resulting in several classifiers that account for the regional heterogeneity in mpMRI [15]. Under a similar Bayesian modeling framework, scalable modeling of the between-voxel correlation for high-dimensional MR classification has also been discussed [16]. Although having provided promising tools for modeling the complex structures of high-dimensional mpMRI data, these Bayesian methods have also shown limitations, such as the inability to handle local features that may cause the spatial heterogeneity across the prostate. Additionally, there is a need to extend binary classification of PCa to more complex classifications, such as detailed categorization of the clinical aggressiveness of PCa based on Gleason Score [5, 8], which will be computationally challenging for Bayesian hierarchical models due to the large amount of model parameters involved.

In this paper, we propose a machine learning-based approach to voxel-wise classification of PCa, which flexibly incorporates the various mpMRI data structures and addresses limitations of the recently proposed Bayesian classification models. The method conducts a multi-resolution modeling approach using ensemble learning via the super learner algorithm [33]. Briefly, we first train a given classification model/algorithm (which we call “base learner”) locally within each sub-region of the prostate under different resolutions. The multi-resolution, sub-region specific learners are then combined for voxel-wise classification of future data. This strategy enables our method to capture both homogeneous/global features and heterogeneous/local features of mpMRI, which is a fundamental improvement compared to previous Bayesian classifiers that can only handle between-anatomic-zone heterogeneity assuming a stationary spatial process. The super learner framework also allows implementation of any types of base learners, which means that the resulting classifier can be continuously updated when novel, superior classification methods are available. We propose to account for between-voxel correlation by applying a spatial Gaussian kernel smoother to the voxel-wise cancer probabilities predicted by the multi-resolution base learners [15, 26, 34]. As opposed to the previous Bayesian spatial models, this spatial smoothing technique is considered due to practical concerns including its minimal computational cost, easy implementation and generally good performance in reducing random noise in the data. We will first introduce the algorithm for classifying binary PCa status. To demonstrate the flexibility of the method in its extension to classifying more complex PCa outcomes, we then discuss how to modify the method to classify the clinical significance

of PCa based on Gleason Score, which is an ordinal outcome that measures the aggressiveness of PCa. Simulation studies and application to our motivating data set were conducted for both binary and ordinal classification, which illustrate the advantages of our proposed method relative to several commonly implemented machine learning approaches.

The rest of the paper is organized as follows. In Section 2, we briefly introduce our motivating data set and notations. In Section 3, we introduce our proposed method and the corresponding algorithm for the binary classification of PCa status, the performance of which is illustrated in Section 4 through simulation studies and application to *in vivo* data. In Section 5, we propose the algorithm for classification of the ordinal, clinical significance of PCa, and discuss its performance on the synthetic and *in vivo* data. Section 6 summarizes the paper and presents a discussion for future directions.

2. Voxel-wise MpMRI data and notations

We first give an overview of our motivating data, which were collected on the voxel level from 34 prostate slices of 34 different patients diagnosed with PCa [16, 25]. Briefly, maps of the quantitative MRI parameters, including apparent diffusion coefficient (ADC), area under the gadolinium concentration time curve at 90 seconds (AUGC90), reflux rate constant (k_{ep}), forward volume transfer constant (K^{trans}), fractional extravascular extracellular space (V_e) and T2 values, were generated. Manually guided annotation for the zonal information (the location of PZ and CG) was conducted on the T2-weighted images. After surgery, the pathologists manually annotated the cancerous areas and their Gleason scores on the histopathology slides, the maps of which were then co-registered with the corresponding maps of the various MRI parameters. Figure 1 shows the image of a prostate slice annotated with voxel-wise binary cancer status and location of the two main zones (PZ and CG).

[Figure 1 about here.]

Current research on voxel-wise detection of PCa using mpMRI mainly focus on binary classification, where prostate voxels are classified as benign or cancerous. Although refined classification of cancerous tissues can provide more detailed guidance for clinical applications, it has almost never been studied on the voxel level. A widely used system for determining PCa aggressiveness is the Gleason grading system, which was originally proposed in 1966, refined in 1977 gaining almost universal acceptance, then updated in 2005 to a version that has been widely used since then [5, 8]. The Gleason grade, which ranges from 3 to 5, describes the degree of abnormality for the organization of PCa cells on histologic examination (5 indicates the most abnormal). Each patient is assigned with two Gleason grades: a primary score, S^a , that describes the predominant pattern, and a secondary score, S^b , that describes the second predominant pattern [14]. The total Gleason score, $S^a + S^b$, is then used to evaluate PCa aggressiveness of the patient. Gleason score 7 tumors show heterogeneity in the biological behavior, with clear differences in prognosis between patients with score 3+4 tumors and patients with score 4+3 tumors at radical prostatectomy [4]. We then utilize this to categorize cancerous tissues into clinically insignificant cancer ($S^a + S^b = 3 + 3$ or $3 + 4$) and clinically significant cancer ($S^a \geq 4$). This results in three ordinal categories of PCa: no PCa, clinically insignificant PCa and clinically significant PCa, which is consistent with newly proposed guidelines for deciding men's eligible for active surveillance [7, 22].

We now introduce notations which will be used to describe the voxel-wise mpMRI data. Assume that there are $N = 34$ patients (i.e. prostate slices), and n_i ($2098 \leq n_i \leq 5756$) voxels in the image of the i -th slice, $i = 1, \dots, N$. For the j -th voxel in the i -th image, a $d \times 1$ vector of quantitative mpMRI parameters, $\mathbf{y}_{ij} = (y_{ij,1}, \dots, y_{ij,d})^T$, is measured. For our motivating data set, we only consider $d = 4$ mpMRI parameters including ADC, AUGC90, k_{ep} and K^{trans} , the combination of which provides the highest average area under the ROC curve (AUC) using the generalized linear model in [25]. Each voxel is annotated with a primary and a secondary Gleason Score, which are denoted as S_{ij}^a and S_{ij}^b , respectively, based on which we define a binary cancer indicator, $c_{ij} = \mathbb{I}(S_{ij}^a + S_{ij}^b \geq 6)$ (1: cancer, 0: noncancer), where $\mathbb{I}(\cdot)$ is the indicator function, and an ordinal outcome for the clinical significance of PCa, G_{ij} , which equals 1 (noncancer) if $S_{ij}^a \leq 3$ and $S_{ij}^a + S_{ij}^b < 6$, 2 (clinically insignificant cancer) if $S_{ij}^a + S_{ij}^b \in \{3+3, 3+4\}$, and 3 (clinically significant cancer) otherwise. The location information of the voxel is described by r_{ij} , an indicator for zone (1: PZ, 0: CG), and \mathbf{s}_{ij} , a 2-D coordinate standardized across all prostate images. Note that there is currently no standard template for prostate due to the variability in size, shape, etc., and therefore we conducted a rough rescaling on the original voxel-wise coordinates to ensure that all images fall into the same support $(-1, 1) \times (-1, 1)$, with $(0, 0)$ being the center of each prostate slice.

3. Methods

Our method was motivated by the need for a flexible and computationally convenient PCa classification approach that can incorporate complex structures of the mpMRI data. Specifically, we propose a two-stage model that incorporates the regional heterogeneity in mpMRI via a super learner framework [33]. In stage one, we first select a base learner, for example, a statistical model or a machine learning algorithm that can classify the voxel-wise PCa status. Next, we segment $(-1, 1) \times (-1, 1)$, the 2-D support of the prostate gland, into $k \times k$ equal-size, rectangular sub-regions using a set of different values for $k \in \mathbb{N}^+$. Under the $k \times k$ resolution, we train the selected base learner locally in each of the k^2 sub-regions. In stage two, we use the classification results from the stage-one, multi-resolution base learners to train a new classifier, which is essentially a weighted combination of the base learners.

3.1. Standard super learner algorithm

We first provide a brief overview of the standard super learner algorithm, which was originally proposed as an ensemble learning-approach for prediction [33]. Super learner constructs an optimal weighted combination of multiple candidate learners using Cross-Validation, which has been shown to perform asymptotically as well as the oracle learner (i.e. the learner that minimizes risk under the true data-generating distribution) in terms of expected risk difference among the family of candidate learners, if the number of candidate learners, K , is polynomial in sample size, n , i.e. $K \leq n^q$ for some $q < \infty$ [33]. Intuitively, the super learner uses ensemble learning to “average” across multiple candidate learners, therefore capturing the characteristics of the data that are revealed by various types of prediction methods.

The standard super learner algorithm proceeds as follows. Suppose we have n i.i.d. observations, $O_i = (X_i, Y_i) \sim F_0$, $i = 1, 2, \dots, n$. The goal is to train a regression

model, $\hat{\psi}_0(X) = E_0(Y|X)$, which is the minimizer of the expectation of a loss function, $E_0 L(O, \psi)$. Note that the super learner is applicable to any parameter that can be defined as the minimizer of a loss function over a parameter space. Assume that there are K candidate prediction models, Ψ_k , $k = 1, 2, \dots, K$, each representing a different mapping from the data, $P_n = \{(Y_i, X_i), i = 1, 2, \dots, n\}$, to the parameter space of the functions of X . A V-fold Cross-Validation is conducted to determine the weight of each candidate learner: suppose that $v \in \{1, 2, \dots, V\}$ denotes a split of the sample that generates an index set of training sample, $T(v)$, and an index set of validation sample, $V(v)$, where $T(v) \cup V(v) = \{1, 2, \dots, n\}$, $\bigcup_{v=1}^V V(v) = \{1, 2, \dots, n\}$ and $V(v_1) \cap V(v_2) = \emptyset$, $\forall v_1 \neq v_2$. For each v , we obtain $\hat{\psi}_{k,v} = \hat{\Psi}_k(P_{n,T(v)})$, i.e. the realization of each Ψ_k on the training set $P_{n,T(v)}$, then apply $\{\hat{\psi}_{k,v}, k = 1, 2, \dots, K\}$ to the corresponding validation set $V(v)$ to get predictions $\{Z_i = (\hat{\psi}_{k,v}(X_i), k = 1, 2, \dots, K)^T, i \in V(v)\}$, so that each sample will have a vector of K Cross-Validated predictions Z_i obtained from the K candidate models. A new data set $\{(Y_i, Z_i), i = 1, 2, \dots, n\}$ is then constructed, with Z_i being the $K \times 1$ vector of new covariates, to train a stage-two model, $\tilde{\Psi}$, which is a mapping from $\{(Y_i, Z_i), i = 1, 2, \dots, n\}$ to $\tilde{\Psi}(\{(Y_i, Z_i), i = 1, 2, \dots, n\}) : \mathcal{Z} \rightarrow \mathcal{Y}$. Given $\tilde{\Psi}$ and $\{\hat{\psi}_{k,v}, k = 1, 2, \dots, K, v = 1, 2, \dots, V\}$, we define a new mapping $\hat{\Psi}^*$ from the original data $P_n = \{(Y_i, X_i), i = 1, 2, \dots, n\}$ to the predictor $\tilde{\Psi}(\{(Y_i, Z_i = (\hat{\Psi}_k(P_{n,T(v_i)})(X_i), k = 1, 2, \dots, K)^T), i = 1, 2, \dots, n\})$. The super learner for a new sample with observation X trained with data P_n is then given by $\hat{\Psi}(P_n)(X) = \hat{\Psi}^*(P_n)(\hat{\Psi}_k(P_n)(X), k = 1, 2, \dots, K)$.

3.2. The proposed algorithm for binary classification of PCa

Our proposed voxel-wise classification algorithm for PCa adopts the idea of super learner to account for regional heterogeneity in the mpMRI data. The basic framework is similar to that of the super learner, but, instead of combining various types of learners, we combine learners of the same type but trained at different resolutions. Suppose the outcome of interest is the voxel-wise, binary PCa status, c_{ij} s. We first select a base learner, Ψ , which can be any classification model/algorithm applicable to the classification problem. We split N subjects into V folds, and for the v -th split, $v = 1, 2, \dots, V$, we divide the subjects into a training set with index $T(v) \subset \{1, 2, \dots, N\}$, that includes data in all but the v -th fold, and a validation set with index $V(v) = \{1, 2, \dots, N\} \setminus T(v)$. Under the v -th split, we first train the base learner using training data on the whole prostate gland (“WG”, which we denote as $A_{1,1}$) and obtain the global learner, $\hat{\Psi}_{1,1}^v(\mathbf{y})$, where \mathbf{y} denotes a vector of the mpMRI parameters. Second, we segment the 2-D support of WG, $(-1, 1) \times (-1, 1)$, into 2×2 equal-size sub-regions: $A_{2,1} = (-1, 0) \times (-1, 0)$, $A_{2,2} = (-1, 0) \times (0, 1)$, $A_{2,3} = (0, 1) \times (-1, 0)$, and $A_{2,4} = (0, 1) \times (0, 1)$. Note that the voxels that fall onto the edge of some sub-regions can be included in any sub-region that share the edge. We train the base learner separately within each sub-region to obtain region-specific learners, $\{\hat{\Psi}_{2,l}^v, l = 1, 2, \dots, 2^2\}$. The trained learner under 2×2 resolution then becomes $\hat{\Psi}_2^v(\mathbf{y}) = \sum_{l=1}^4 \mathbb{I}(\mathbf{s} \in A_{2,l}) \hat{\Psi}_{2,l}^v(\mathbf{y})$, where \mathbf{s} denotes the coordinate of a voxel. Third, we segment the support of WG into 3×3 equal-size sub-regions: $\{A_{3,l} = (a, a + 2/3) \times (b, b + 2/3), a, b = -1, -1/3, 1/3, l = 1, 2, \dots, 3^2\}$, train the base learner within each region and get $\{\hat{\Psi}_{3,l}^v, l = 1, 2, \dots, 3^2\}$. The trained learner under 3×3 resolution is then $\hat{\Psi}_3^v(\mathbf{y}) = \sum_{l=1}^9 \mathbb{I}(\mathbf{s} \in A_{3,l}) \hat{\Psi}_{3,l}^v(\mathbf{y})$. Theoretically, we can continue this segmentation process with $k = 4, 5, 6$, etc. In this

paper, we consider $k \in \{1, 2, 3\}$, i.e. the lowest $K = 3$ resolutions, for illustration. Figure 2 illustrates the corresponding region segmentation on three prostate images in our data.

[Figure 2 about here.]

After training the model under $k \times k$ resolution, we apply $\{\widehat{\Psi}_k^v, v = 1, 2, \dots, V\}$ to the corresponding validation sets, which gives us the Cross-Validated classification results, $x_{ij}^k = \sum_{v=1}^V \mathbb{I}(i \in V(v)) \widehat{\Psi}_k^v(\mathbf{y}_{ij})$. Before combining results at different resolutions, we would like to take into account the spatial dependency between voxels. Formal spatial modeling can be conducted, which, however, has been shown to suffer from computational burden even with appropriate dimension reduction techniques [16]. To avoid large computational cost, we propose to implement the computationally efficient spatial smoothing instead. Specifically, we apply the Nadaraya-Watson estimator with Gaussian kernel [26, 34] to $\{x_{ij}^k, j = 1, 2, \dots, n_i\}$ separately for each image i , and obtain a vector of spatially smoothed, Cross-Validated classification results for each voxel: $\tilde{\mathbf{x}}_{ij} = (\tilde{x}_{ij}^1, \tilde{x}_{ij}^2, \dots, \tilde{x}_{ij}^K)^T$. We then develop a stage-two classification model, Φ , using $\tilde{\mathbf{x}}_{ij}$ s as the inputs. Given that the outcome is binary, a generalized linear model with a probit link function is adopted. Finally, we train the stage-one, multi-resolution base learners, Ψ_k s, on the entire data set, which, combined with the intermediate spatial smoothing and the trained stage-two model $\widehat{\Phi}$, becomes the final classifier.

[Figure 3 about here.]

Figure 3 summarizes the workflow of the proposed binary classification algorithm, from which we can observe two attractive features. First, it efficiently accounts for both global and complex local mpMRI structures via multi-resolution modeling. Second, it can implement any classification methods, even “black-box” machine learning algorithms, as the base learner. Currently, we only consider combining the three lowest resolutions for illustration, but the segmentation process can continue to finer resolutions depending on the original resolution of the mpMRI images and the locality of region heterogeneity. A practical concern is that, under finer-resolution segmentations, some generated sub-regions may only have cancer or non-cancer voxels, making the model training difficult, and thus the upper limit of the resolutions for region segmentation should be chosen to minimize the number of such single-class sub-regions. However, we would like to note that with only a few single-class sub-regions, the algorithm can still be implemented: suppose that under segmentation of the highest resolution $K \times K$, all voxels in one sub-region, A_{K,l^*} , are of the same cancer status $c \in \{0, 1\}$. We then define $\widehat{\Psi}_{K,l^*}(\mathbf{y}) \equiv c$, i.e. new voxels in this sub-region will be classified as c with probability 1. Note that this classification result will be averaged with the results from lower-resolution classifiers that do not have this single-class issue, resulting in a classifier that is not uniformly equal to c for all voxels in this sub-region.

4. Application

4.1. Simulation studies

We first conducted simulations to illustrate the performance of the proposed binary classification algorithm. We considered multiple choices for the base learner, including generalized linear model with probit link function (“GLM”), quadratic discriminant analysis (“QDA”, [31]) and random forest (“RF”, [11]). Given each base learner,

we applied the following classifiers: (1) “Baseline”: the base learner; (2) “SL0”: the proposed algorithm without the spatial smoothing step; and (3) “SL”: the proposed algorithm. We assessed the improvement due to our proposed multi-resolution modeling strategy by comparing between classifiers (1) and (2), and the improvement due to spatial smoothing by comparing between classifiers (2) and (3). Additionally, we considered another classifier, “GLM + QDA + RF”, which combines results from the multi-resolution GLM, QDA and RF together using super learner. For this classifier, we also considered either implementing or not implementing spatial smoothing (“SL” and “SL0”, respectively).

The synthetic data were generated as follows. The shapes of the simulated prostate images, including the voxel-wise zone indicators r_{ij} s and standardized 2-D coordinates s_{ij} s, were selected with replacement from those of the images in the motivating data set. Within each image, the voxel-wise cancer status and mpMRI parameters were simulated according to model (1):

$$\begin{aligned} \mathbf{w}_i &\sim \mathcal{MVN}(\mathbf{0}, \mathbf{C}(\mathbf{S}_i, \mathbf{S}_i | \boldsymbol{\theta})), \quad c_{ij}^* \sim N(q_{r_{ij},0} + w_{ij}, 1), \\ c_{ij} &= I(c_{ij}^* > 0), \quad \mathbf{e}_{i_k}^k \sim \mathcal{MVN}(\mathbf{0}, \boldsymbol{\Lambda}), \\ \mathbf{y}_{ij} &\stackrel{ind}{\sim} \mathcal{MVN}(\boldsymbol{\mu}_{c_{ij},r_{ij}} + \sum_{k=1}^K \mathbf{e}_{i_k}^k + \boldsymbol{\delta}_i, \boldsymbol{\Gamma}_{c_{ij},r_{ij}}). \end{aligned} \quad (1)$$

Specifically, to introduce spatial correlation between voxel-wise cancer status within each image i , we simulated a vector of spatially correlated random effects, $\mathbf{w}_i = (w_{i,1}, \dots, w_{i,n_i})^T$, from a multivariate normal distribution assuming a Matérn correlation structure, i.e. the (i, j) -th entry of the spatial covariance matrix, $\mathbf{C}(\mathbf{S}_i, \mathbf{S}_i | \boldsymbol{\theta})$, was defined as $\mathbf{C}(\mathbf{s}_{ij}, \mathbf{s}_{ik} | \boldsymbol{\theta}) = \frac{\sigma^2}{2^{\nu-1}\Gamma(\nu)} \left(\frac{2\nu^{1/2}\|\mathbf{s}_{ij} - \mathbf{s}_{ik}\|}{\phi} \right)^\nu \times \mathbf{J}_\nu \left(\frac{2\nu^{1/2}\|\mathbf{s}_{ij} - \mathbf{s}_{ik}\|}{\phi} \right)$, where $\boldsymbol{\theta} = \{\sigma^2, \phi, \nu\}$. Second, we simulated c_{ij}^* s independently from $N(q_{r_{ij},0} + w_{ij})$ s, where $q_{r_{ij},0}$ denotes the probit of cancer prevalence in zone $r_{ij} \in \{0, 1\}$, and then simulated $c_{ij} = \mathbb{I}(c_{ij}^* > 0)$ according to the probit model. We assumed that the distribution of the mpMRI parameters, \mathbf{y}_{ij} , varied by cancer status c_{ij} and zone indicator r_{ij} with mean $\boldsymbol{\mu}_{c_{ij},r_{ij}}$ and covariance $\boldsymbol{\Gamma}_{c_{ij},r_{ij}}$. To introduce heterogeneity across multi-resolution sub-regions, we added region-specific random shifts, $\{\mathbf{e}_{i_k}^k \sim \mathcal{MVN}(\mathbf{0}, \boldsymbol{\Lambda}), k = 1, \dots, K, i_k = 1, \dots, k^2\}$, on \mathbf{y}_{ij} , with i_k denoting the indicator for sub-region under $k \times k$ segmentation, and i_{ij}^k denoting the indicator for the sub-region the j -th voxel in the i -th image belongs to under $k \times k$ segmentation.

We set the mean and covariance of the mpMRI parameters, as well as cancer prevalence in the PZ and CG, equal to their estimates from the motivating data set. We varied $q_{r,0}$ s and $\boldsymbol{\Lambda}$ to simulate either moderate or strong regional heterogeneity. We also varied $\boldsymbol{\theta} = \{\sigma^2, \phi, \nu\}$ to simulate either moderate or strong correlation between voxels within each image. Detailed simulation settings are summarized in Appendix A.1 of the supplementary materials. The spatial Gaussian kernel smoothing bandwidth was selected via Cross-Validation to maximize the AUC of each base learner under each resolution. We conducted 5-fold Cross-Validation on 34 synthetic subjects in each simulation, and summarized classification results under each simulated scenario based on 100 simulations.

[Table 1 about here.]

Simulation results are summarized by the empirical mean and standard deviation (SD) of the AUC, S80 and S90 (sensitivity corresponding to 80% and 90% speci-

ficity, respectively), under moderate (Table S1 in Appendix B of the supplementary materials) and strong (Table 1) regional heterogeneity, respectively. Among the three considered base learners, GLM and QDA both outperform RF and show similar classification accuracy. Our proposed multi-resolution modeling strategy improves the AUC, S80 and S90 of the base learner (“SL0” v.s. “baseline”), and the improvement increases as the magnitude of regional heterogeneity increases. The multi-resolution modeling strategy also substantially reduces the SD of AUC, S80 and S90 in all simulation settings. The intermediate spatial smoothing step further improves classification, where the improvement increases as the magnitude, scale and smoothness of the spatial correlation increase (“SL” v.s. “SL0”). Implementing spatial smoothing inflates the SD of AUC, S80 and S90 obtained from SL, but the SD remains smaller than that of the base learner. Without the intermediate spatial smoothing step, combining GLM, QDA and RF (GLM + QDA + RF) provides similar classification accuracy as the best single learner-based classifier (see “SL0”s in Tables S1 and Table 1). After incorporating spatial smoothing, however, GLM + QDA + RF leads to improved classification compared to the single learner-based classifiers with spatial smoothing (see “SL”s in Tables S1 and Table 1).

*4.2. Application to *in vivo* data*

We now show performance of the various binary classifiers on our motivating data set described in Section 2. Table 2 summarizes classification results obtained from 5-fold Cross-Validation. When using GLM as the base learner, the proposed multi-resolution modeling approach improves the AUC from 0.735 to 0.775, the S80 from 0.582 to 0.651, and the S90 from 0.423 to 0.514. The intermediate spatial smoothing step further improves the AUC to 0.819, the S80 to 0.728, and the S90 to 0.590. Similar improvements can be observed when using QDA or RF as the base learner. Without the intermediate spatial smoothing step, the proposed algorithm using GLM or QDA as the base learner provides higher classification accuracy than when using RF as the base learner (AUC: 0.775 and 0.761 v.s. 0.738). But after incorporating spatial smoothing, the RF-based super learner performs better than the GLM and QDA-based learners (AUC: 0.836 v.s. 0.819 and 0.803).

[Table 2 about here.]

An interesting finding is that, without the intermediate spatial smoothing step, combining the multi-resolution GLM, QDA and RF-based learners has an AUC slightly higher than but similar to that of the best single learner-based classifier (0.778 for GLM + QDA + RF v.s. 0.775 for GLM, 0.761 for QDA and 0.738 for RF). But after adding the spatial smoothing step, the RF-based super learner provides higher classification accuracy than GLM + QDA + RF (AUC: 0.836 v.s. 0.825). This could be explained by the possibility that spatial smoothing reduces variation due to spatial correlation and random noise, but after combining GLM, QDA, and RF-based learners together, most of the noises in the data that would otherwise be reduced by spatial smoothing have already been removed, and, as a result, there is less room for improvement. Table 2 also reports the estimated weights for each resolution, i.e. the estimated coefficients in the stage-two model averaged across the 5 folds of Cross-Validation. We can observe that, although different resolutions have different weights, the magnitude of the weights are similar. This indicates that the base learners trained under the three different resolutions have all made contributions to the classification, which explains why our

multi-resolution modeling approach outperforms the global classifiers.

5. Extension to classifying ordinal clinical significance of PCa

The development of the proposed algorithm was motivated by the need for an approach that could be easily extended to tackle more complex classification/prediction problems for PCa. In this Section, we will discuss an extension of our proposed algorithm to classifying the ordinal outcome G defined in Section 2, i.e. the clinical significance of PCa, which is critical for selecting appropriate treatment in clinical practice.

5.1. Method

Recall that the voxel-wise indicator for clinical significance of PCa is defined based on Gleason Score: $G = 1$ (noncancer) if $S^a < 3$ and $S_a + S_b < 6$, $G = 2$ (clinically insignificant cancer) if $S_a + S_b = 3+3$ or $3+4$, and $G = 3$ (clinically significant cancer) if otherwise. Here G_{ij} s have $Z = 3$ ordered levels. In a more general situation where, for example, we would like to predict the Gleason Score directly, Z can have larger values. Implementation of the ordinal classification algorithm still follows the workflow proposed for binary classification in Section 3.2, but with the following modifications. First, the selected base learners are the classifiers that can handle ordinal outcomes, such as ordinal probit regression. Second, given the ordinal outcome, there are multiple choices for $\tilde{\mathbf{x}}_{ij}$, i.e. the stage-one output that summarizes classification results of the multi-resolution base learners, which will also be used as the covariates in stage-two model. For example, $\tilde{\mathbf{x}}_{ij}$ can be the vector of the predicted probabilities for any two of the three categories, or simply the predicted category, \hat{G}_{ij} . Third, we change the stage-two model from probit regression to ordered probit regression:

$$G_{ij} = z \text{ if } a_{z-1} \leq G_{ij}^* < a_z, \quad z = 1, 2, \dots, Z,$$

where $\{a_z, z = 0, 1, \dots, Z\}$ is the set of boundaries between categories, with $a_0 = -\infty$ and $a_Z = \infty$.

One practical issue that adds difficulty to ordinal PCa classification is the large difference in prevalence across different PCa categories. Take the motivating data set as an example: the prevalence of noncancer ($G = 1$), clinically insignificant ($G = 2$) and significant ($G = 3$) cancer voxels are 0.833, 0.058 and 0.109, respectively, and, as a result, detecting the less prevalent clinically insignificant and significant PCa voxels can be challenging with limited information provided by the data. To increase the power of detecting less prevalent PCa voxels, we consider a weighted likelihood approach for the stage-two model [1, 13]:

$$L^w(\mathbf{G}|\boldsymbol{\vartheta}) = \prod_{i=1}^N \prod_{j=1}^{n_i} f(G_{ij}|\tilde{\mathbf{x}}_{ij}, \boldsymbol{\vartheta})^{w_{ij}(G_{ij}, \tilde{\mathbf{x}}_{ij})}, \quad (2)$$

where $\boldsymbol{\vartheta}$ denotes the set of model parameters, and w_{ij} is a user-defined weight for the j -th voxel in the i -th image that is a bounded differentiable non-negative function of G_{ij} and $\tilde{\mathbf{x}}_{ij}$. The standard likelihood is equivalent to the weighted likelihood with equal weights “ W_1 ”: $w_{ij} = 1/\sum_{i=1}^N n_i$, $\forall i, j$. An option for unequal weights is “ W_2 ”: $w_{ij} = 1/(m_{G_{ij}} Z)$, where m_z denotes the number of voxels that belong to category

$z \in \{1, 2, 3\}$. Based on this definition, w_{ij} is inversely proportional to the prevalence of the corresponding category G_{ij} , and therefore we up-weight the data for rare categories and down-weight the data for more prevalent categories. This definition of weight is reasonable for classification when missing aggressive disease is deemed as a bigger issue than other types of false classifications.

Two metrics for assessing the accuracy of ordinal classification are $Z \times Z$ classification table and overall error rate (i.e. the percentage of the falsely categorized voxels). Additionally, to evaluate the classification results for each category, we define: (1) “False Positive Rate” for category z : $\text{FPR}(z)$, the percentage of the voxels in category z that are falsely classified as $z' \neq z$; (2) “False Discovery Rate” for category z : $\text{FDR}(z)$, the percentage of the voxels classified as in z that are actually not in z :

$$\begin{aligned}\text{FPR}(z) &= \frac{\sum_{i=1}^N \sum_{j=1}^{n_i} \mathbb{I}(G_{ij} = z, \hat{G}_{ij} \neq z)}{\sum_{i=1}^N \sum_{j=1}^{n_i} \mathbb{I}(G_{ij} = z)}, \\ \text{FDR}(z) &= \frac{\sum_{i=1}^N \sum_{j=1}^{n_i} \mathbb{I}(G_{ij} \neq z, \hat{G}_{ij} = z)}{\sum_{i=1}^N \sum_{j=1}^{n_i} \mathbb{I}(\hat{G}_{ij} = z)}.\end{aligned}\quad (3)$$

5.2. Simulation studies

We conducted simulations to evaluate the performance of our proposed algorithm for classifying the ordinal clinical significance of PCa. Detailed simulation settings are summarized in Appendix A.2 of the supplementary materials. We set the between-class boundaries, a_1 and a_2 , equal to the median and 70-th percentile, respectively, of the simulated G_{ij}^* s, i.e. we assign a high prevalence (50%) to the noncancer voxels, a low prevalence (20%) to the clinically significant cancer voxels, and the lowest prevalence (10%) to the clinically insignificant cancer voxels to mimic the scenario observed in the motivating data set. The generating process for \mathbf{w}_{is} , G_{ij}^* s, $q_{r,0s}$, $\mathbf{e}_{i_k}^k$ s, $\boldsymbol{\delta}_i$ s and \mathbf{y}_{ij} s was similar to that in Section 4.1, except that \mathbf{y}_{ij} depended on G_{ij} instead of c_{ij} .

We considered different choices for the base learner, including ordered probit regression (“GLM”), QDA, and RF. For the weighted likelihood of the stage-two model, we implemented two different sets of weights previously discussed in Section 5.1: (1) equal weights “ W_1 ”; (2) unequal weights “ W_2 ” that are inversely proportional to the prevalence of the corresponding cancer categories. Given each base learner, we applied the following models: (1) “Baseline”: the base learner; (2) “SL0 + W_1 ”: the proposed algorithm without spatial smoothing and with weights W_1 ; (3) “SL + W_1 ”: the proposed algorithm with weights W_1 ; (4) “SL0 + W_2 ”: the proposed algorithm without spatial smoothing and with weights W_2 ; and (5) “SL + W_2 ”: the proposed algorithm with weights W_2 . Additionally, we considered combining the stage-one, multi-resolution GLM, QDA and RF (“GLM + QDA + RF”) either with or without spatial smoothing, and using either W_1 or W_2 as the weights (“SL0 + W_1 ”, “SL + W_1 ”, “SL0 + W_2 ” and “SL + W_2 ”, respectively). As previously discussed, there are multiple choices for $\tilde{\mathbf{x}}_{ij}$ s, the stage-one output that will be used as the covariates for stage-two model. In the simulation, we used the predicted probabilities for the first two categories as $\tilde{\mathbf{x}}_{ij}$ s to illustrate the performance of the method. The tuning parameters of the selected base learners were selected via Cross-Validation to minimize the overall error rate. We also used Cross-Validation to select the spatial Gaussian kernel smoothing bandwidth that minimized the overall error rate under each resolution. In each simulation, results

were summarized by 4-fold Cross-Validation on 40 subjects. We summarized the results by the aforementioned classification table, overall error rate, as well as the FPR and FDR for each cancer category.

[Table 3 about here.]

Table 3 presents simulation results assuming strong regional heterogeneity and strong between-voxel correlation using GLM as the base learner. Results assuming weaker between-voxel correlation and weaker regional heterogeneity are reported in Tables S2 and S3, respectively, in Appendix C.1 of the supplementary materials. The reported results are averaged across 100 simulations per scenario. By comparing $SL_0 + W_1$ to Baseline, we observe that the proposed multi-resolution modeling strategy improves the classification for categories 1 and 3, with larger improvement when there is stronger regional heterogeneity. Comparing $SL + W_1$ to $SL_0 + W_1$, the spatial smoothing step further improves classification of the two categories, with larger improvement under stronger spatial correlation. Overall, the number of correctly identified clinically significant cancer voxels has a large increase from Baseline to the four models using the proposed algorithm. We also considered using QDA or RF as the base learner, or combining multi-resolution GLM, QDA and RF, the simulation results for which are summarized in Tables S4-S9 in Appendix C.1 of the supplementary materials. In general, using GLM, QDA or RF as the base learner gives similar classification results, while combining multi-resolution GLM, QDA and RF together provides similar or potentially higher classification accuracy for all categories compared to any single learner-based classifiers.

One noticeable finding, the rationale for which was briefly discussed in Section 5.1, is that correctly identifying clinically insignificant cancer voxels is challenging. When using GLM as the base learner, both the baseline model and our proposed algorithm with equal weights W_1 cannot identify any clinically insignificant cancer voxels; although QDA and RF can correctly identify a small proportion, the corresponding super learners with equal weights W_1 fail to identify any, even though better overall performance is achieved. Both the baseline model and our proposed algorithm using equal weights sacrifice classification of the less prevalent clinically insignificant cancer category to improve the overall classification. However, with weights W_2 that up-weight less prevalent cancer categories, the multi-resolution modeling approach substantially improves the detection of the clinically insignificant cancer voxels, which, however, comes with the price of higher FPR for noncancer voxels, although the FDR of noncancer voxels is lowered. While our algorithm with unequal weights W_2 does not improve the overall ordinal classification, its enhanced ability of identifying cancerous voxels can be an appealing feature in clinical practice. The spatial smoothing step, on the other hand, has further improved classification for all categories using either W_1 or W_2 as the weights. Note that the challenge in distinguishing clinically insignificant cancer from the other two categories comes not only from the low prevalence of the category, but also from the fact that the differences in sample mean of the mpMRI parameters between different categories are quite small considering the large sample variance, which is possibly due to the limited sample size that is commonly observed from most of the current mpMRI studies [18]. As long as we only use the voxel-wise, category-specific distribution of the mpMRI parameters to distinguish between cancer categories, this issue will always exist and cannot be simply addressed by the multi-resolution modeling strategy.

5.3. Application to *in vivo* data

We applied the ordinal classifiers, including Baseline, $SL0 + W_1$, $SL + W_1$, $SL0 + W_2$, and $SL + W_2$, using ordinal probit regression (“GLM”) as the base learner to our motivating data set. Tables 4 and 5 summarize the 4-fold Cross-Validated results using predicted probabilities of the first two categories and the predicted cancer categories, respectively, as \tilde{x}_{ij} (the stage-one output). Compared to Baseline, we see that the proposed multi-resolution modeling approach with equal weights ($SL0 + W_1$) gives lower overall error rates, FPR and FDR for the clinically significant cancer voxels, lower FDR and slightly higher FPR for the noncancer voxels, and still no identified clinically insignificant cancer voxels. Comparing $SL + W_1$ to $SL0 + W_1$, the spatial smoothing step leads to further improvements in the aforementioned directions. Comparing $SL + W_1$ to $SL + W_2$, we observe that using unequal weights W_2 enables our proposed algorithm to correctly identify some clinically insignificant cancer voxels. However, it leads to higher FPR for the noncancer voxels as well, although the corresponding FDR is lowered. With equal weights W_1 , using predicted probabilities and using classified categories as the stage-one output give similar results. With unequal weights W_2 , compared to using the classified categories as the stage-one output, using predicted probabilities tends to identify more clinically significant and insignificant cancer voxels, with lower FPR for both categories, but also higher FDR for the two categories, higher FPR for the noncancer voxels, and higher overall error rate.

[Table 4 about here.]

[Table 5 about here.]

We also considered using QDA or RF as the base learner, or combining the multi-resolution GLM, QDA and RF. Results are summarized in Tables S10-S12 in the Online Appendix C.2 of the supplementary materials. Overall, using GLM, QDA or RF as the base learner gives similar results, while combining GLM, QDA and RF together improves the detection of both clinically insignificant and significant PCa voxels, but decreased FPR for noncancer and higher overall error rate.

6. Discussion

We propose a novel classification algorithm for the voxel-wise detection and grading of PCa using mpMRI data. The main feature of the algorithm is the multi-resolution modeling strategy, which accounts for regional heterogeneity in the mpMRI data by averaging over global and local classifiers trained at different resolutions via super learner. This multi-resolution modeling strategy provides a flexible and easily implementable approach to capturing both global and local features of mpMRI, addressing limitations of the Bayesian hierarchical models recently proposed for voxel-wise classification of binary PCa status. We also propose to conduct spatial Gaussian kernel smoothing to further reduce noise in the presence of strong between-voxel correlation, considering its promising performance and computational efficiency compared to the Bayesian spatial models [16]. Different from the Bayesian hierarchical modeling framework, our proposed algorithm can implement any classifiers, including the black-box machine learning algorithms, as the base learners. We have demonstrated the advantages of our algorithm over the conventional classification methods such as GLM, QDA and RF on synthetic and real patient data. Additionally, our algorithm can combine

multiple types of classifiers, which has the potential to further improve classification, thus providing a flexible modeling framework that can be continuously enhanced and updated.

An important feature of our proposed algorithm is the easy extension to more complex classification problems. As an illustration, we extended the algorithm to classification of the ordinal clinical significance of PCa. Improvements in detecting clinically significant PCa were shown by both simulations and application to real patient data, which means that potentially enhanced guidance for clinical treatment can be achieved. We propose to use weighted likelihood for the stage-two model in our algorithm to improve classification of the less prevalent cancer categories. Depending on the primary goal, the weights can be adjusted to enhance detection of some specific cancer categories.

Although our proposed classifiers outperform the base learners for identifying clinically significant and insignificant cancer voxels, the resulting classification accuracy is still expected to be relatively low. A crucial reason is that most of the existing voxel-wise classifiers distinguish between different cancer categories by the voxel-level, category-specific distribution of the mpMRI parameters, which, due to the limited number of patients available in most of the mpMRI studies, has small difference between categories that is hard to detect given the large sample variance. In order to achieve fundamentally improved ordinal classification of PCa under the current sample size, novel modeling approaches should be developed to replace the existing voxel-wise modeling approaches. For example, a two-step, region-wise modeling approach can be considered, where we first locate candidate cancer lesions based on voxel-wise classification, then determine their aggressiveness by their similarity to areas of each cancer category in terms of lesion-wise mpMRI structures. Our super learner algorithm can also be extended to incorporate more complex model assumptions. We currently assume that the weight for each resolution is constant across the whole prostate gland. Alternately, we can allow the weights to vary by the location in a prostate. Additionally, instead of a post-hoc procedure, the spatial smoothing process can be incorporated in the modeling process, which, however, may diminish scalability of the resulting classifier and thus needs careful investigation.

Funding

This work was supported by NCIR01 CA155268, NCIP30 CA077598, NIBIBP41 EB015894, and the Assistant Secretary of Defense for Health affairs, through the Prostate Cancer Research Program under Award No. W81XWH-15-1-0478. Opinions, interpretations, conclusions, and recommendations are those of the author and are not necessarily endorsed by the Department of Defense.

References

- [1] C. Agostinelli and L. Greco, *Weighted likelihood in Bayesian inference*, in *Proceedings of the 46th Scientific Meeting of the Italian Statistical Society*. 2012.
- [2] American Cancer Society, *Key Statistics for Prostate Cancer*, <https://www.cancer.org/cancer/prostate-cancer/about/key-statistics.html> (2019). Accessed: 2019-04-15.

- [3] Y. Artan, M.A. Haider, D.L. Langer, T.H. Van der Kwast, A.J. Evans, Y. Yang, M.N. Wernick, J. Trachtenberg, and I.S. Yetik, *Prostate cancer localization with multispectral MRI using cost-sensitive support vector machines and conditional random fields*, IEEE Transactions on Image Processing 19 (2010), pp. 2444–2455.
- [4] T.Y. Chan, A.W. Partin, P.C. Walsh, and J.I. Epstein, *Prognostic significance of gleason score 3+ 4 versus gleason score 4+ 3 tumor at radical prostatectomy*, Urology 56 (2000), pp. 823–827.
- [5] B. Delahunt, R.J. Miller, J.R. Srigley, A.J. Evans, and H. Samaratunga, *Gleason grading: past, present and future*, Histopathology 60 (2012), pp. 75–86.
- [6] L. Dickinson, H.U. Ahmed, C. Allen, J.O. Barentsz, B. Carey, J.J. Futterer, S.W. Heijmink, P.J. Hoskin, A. Kirkham, A.R. Padhani, *et al.*, *Magnetic resonance imaging for the detection, localisation, and characterisation of prostate cancer: recommendations from a European consensus meeting*, European urology 59 (2011), pp. 477–494.
- [7] J.I. Epstein, *An update of the Gleason grading system*, The Journal of urology 183 (2010), pp. 433–440.
- [8] J.I. Epstein, W.C. Allsbrook Jr, M.B. Amin, L.L. Egevad, I.G. Committee, *et al.*, *The 2005 International Society of Urological Pathology (ISUP) consensus conference on Gleason grading of prostatic carcinoma*, The American journal of surgical pathology 29 (2005), pp. 1228–1242.
- [9] D. Fehr, H. Veeraraghavan, A. Wibmer, T. Gondo, K. Matsumoto, H.A. Vargas, E. Sala, H. Hricak, and J.O. Deasy, *Automatic classification of prostate cancer Gleason Scores from multiparametric magnetic resonance images*, Proceedings of the National Academy of Sciences 112 (2015), pp. E6265–E6273.
- [10] K. Garcia-Reyes, N.M. Passoni, M.L. Palmeri, C.R. Kauffman, K.R. Choudhury, T.J. Poldrack, and R.T. Gupta, *Detection of prostate cancer with multiparametric MRI (mpMRI): effect of dedicated reader education on accuracy and confidence of index and anterior cancer diagnosis*, Abdominal imaging 40 (2015), pp. 134–142.
- [11] T. Hastie, R. Tibshirani, and J. Friedman, *The elements of statistical learning: data mining, inference, and prediction*, Springer Series in Statistics (2009).
- [12] J.V. Hegde, R.V. Mulkern, L.P. Panych, F.M. Fennessy, A. Fedorov, S.E. Maier, and C.M. Temppany, *Multiparametric MRI of prostate cancer: an update on state-of-the-art techniques and their performance in detecting and localizing prostate cancer*, Journal of magnetic resonance imaging 37 (2013), pp. 1035–1054.
- [13] F. Hu and J.V. Zidek, *The weighted likelihood*, Canadian Journal of Statistics 30 (2002), pp. 347–371.
- [14] C. Jensen, J. Carl, L. Boesen, N.C. Langkilde, and L.R. Østergaard, *Assessment of prostate cancer prognostic Gleason grade group using zonal-specific features extracted from biparametric MRI using a KNN classifier*, Journal of applied clinical medical physics 20 (2019), pp. 146–153.
- [15] J. Jin, L. Zhang, E. Leng, G.J. Metzger, and J.S. Koopmeiners, *Detection of prostate cancer with multiparametric MRI utilizing the anatomic structure of the prostate*, Statistics in medicine 37 (2018), pp. 3214–3229.
- [16] J. Jin, L. Zhang, E. Leng, G.J. Metzger, and J.S. Koopmeiners, *Bayesian spatial models for voxel-wise prostate cancer classification using multi-parametric MRI data* (2020).
- [17] F. Khalvati, A. Wong, and M.A. Haider, *Automated prostate cancer detection via comprehensive multi-parametric magnetic resonance imaging texture feature models*, BMC medical imaging 15 (2015), p. 27.
- [18] G. Lemaître, R. Martí, J. Freixenet, J.C. Vilanova, P.M. Walker, and F. Meriaudeau, *Computer-Aided detection and diagnosis for prostate cancer based on mono and multi-parametric MRI: a review*, Computers in biology and medicine 60 (2015), pp. 8–31.
- [19] G. Litjens, O. Debats, J. Barentsz, N. Karssemeijer, and H. Huisman, *Computer-aided detection of prostate cancer in MRI*, IEEE transactions on medical imaging 33 (2014), pp. 1083–1092.
- [20] X. Liu, D.L. Langer, M.A. Haider, Y. Yang, M.N. Wernick, and I.S. Yetik, *Prostate cancer*

segmentation with simultaneous estimation of Markov random field parameters and class, IEEE Transactions on Medical Imaging 28 (2009), pp. 906–915.

[21] R. Lopes, A. Ayache, N. Makni, P. Puech, A. Villers, S. Mordon, and N. Betrouni, *Prostate cancer characterization on MR images using fractal features*, Medical physics 38 (2011), pp. 83–95.

[22] A. Matoso and J.I. Epstein, *Defining clinically significant prostate cancer on the basis of pathological findings*, Histopathology 74 (2019), pp. 135–145.

[23] L. Matulewicz, J.F. Jansen, L. Bokacheva, H.A. Vargas, O. Akin, S.W. Fine, A. Shukla-Dave, J.A. Eastham, H. Hricak, J.A. Koutcher, *et al.*, *Anatomic segmentation improves prostate cancer detection with artificial neural networks analysis of 1H magnetic resonance spectroscopic imaging*, Journal of Magnetic Resonance Imaging 40 (2014), pp. 1414–1421.

[24] S. Mazzetti, M. De Luca, C. Bracco, A. Vignati, V. Giannini, M. Stasi, F. Russo, E. Armando, S. Agliozzo, and D. Regge, *A CAD system based on multi-parametric analysis for cancer prostate detection on DCE-MRI*, Medical Imaging 2011: Computer-Aided Diagnosis 7963 (2011), p. 79633Q.

[25] G.J. Metzger, C. Kalavagunta, B. Spilseth, P.J. Bolan, X. Li, D. Hutter, J.W. Nam, A.D. Johnson, J.C. Henriksen, L. Moench, *et al.*, *Detection of Prostate Cancer: Quantitative Multiparametric MR Imaging Models Developed Using Registered Correlative Histopathology*, Radiology 279 (2016), pp. 805–816.

[26] E.A. Nadaraya, *On estimating regression*, Theory of Probability & Its Applications 9 (1964), pp. 141–142.

[27] E. Niaf, O. Rouvière, F. Mège-Lechevallier, F. Bratan, and C. Lartizien, *Computer-aided diagnosis of prostate cancer in the peripheral zone using multiparametric MRI*, Physics in Medicine & Biology 57 (2012), p. 3833.

[28] Y. Peng, Y. Jiang, T. Antic, M.L. Giger, S. Eggener, and A. Oto, *A study of T2-weighted MR image texture features and diffusion-weighted MR image features for computer-aided diagnosis of prostate cancer*, in *Proc. SPIE*, Vol. 8670. 2013, p. 86701H.

[29] P. Puech, N. Betrouni, N. Makni, A.S. Dewalle, A. Villers, and L. Lemaitre, *Computer-assisted diagnosis of prostate cancer using dce-mri data: design, implementation and preliminary results*, International journal of computer assisted radiology and surgery 4 (2009), pp. 1–10.

[30] V. Shah, B. Turkbey, H. Mani, Y. Pang, T. Pohida, M.J. Merino, P.A. Pinto, P.L. Choyke, and M. Bernardo, *Decision support system for localizing prostate cancer based on multiparametric magnetic resonance imaging*, Medical physics 39 (2012), pp. 4093–4103.

[31] A. Tharwat, *Linear vs. quadratic discriminant analysis classifier: a tutorial*, International Journal of Applied Pattern Recognition 3 (2016), pp. 145–180.

[32] P. Tiwari, J. Kurhanewicz, and A. Madabhushi, *Multi-kernel graph embedding for detection, Gleason grading of prostate cancer via MRI/MRS*, Medical image analysis 17 (2013), pp. 219–235.

[33] M.J. Van der Laan, E.C. Polley, and A.E. Hubbard, *Super learner*, Statistical applications in genetics and molecular biology 6 (2007).

[34] G.S. Watson, *Smooth regression analysis*, Sankhyā: The Indian Journal of Statistics, Series A (1964), pp. 359–372.

Table 1. Simulation results of binary PCa classification assuming strong regional heterogeneity.

Spatial Correlation	Base Learner	Method	Classification Results		
			AUC	S80	S90
Moderate $\sigma^2 = 4$ $\phi = 0.2$ $\nu = 0.8$	GLM	Baseline	.747 (.035)	.544 (.065)	.382 (.068)
		SL0	.829 (.005)	.697 (.009)	.544 (.010)
		SL	.842 (.010)	.732 (.019)	.575 (.022)
	QDA	Baseline	.750 (.033)	.548 (.063)	.386 (.065)
		SL0	.836 (.005)	.710 (.009)	.560 (.011)
		SL	.847 (.010)	.744 (.019)	.589 (.022)
	RF	Baseline	.789 (.014)	.621 (.028)	.460 (.030)
		SL0	.820 (.005)	.685 (.006)	.532 (.006)
		SL	.852 (.006)	.751 (.013)	.593 (.016)
Strong $\sigma^2 = 10$ $\phi = 0.5$ $\nu = 1.5$	GLM + QDA + RF	SL0	.838 (.004)	.714 (.007)	.564 (.008)
		SL	.864 (.006)	.775 (.012)	.622 (.015)
	GLM	Baseline	.746 (.040)	.542 (.073)	.380 (.074)
		SL0	.829 (.005)	.697 (.010)	.543 (.012)
		SL	.920 (.012)	.880 (.024)	.773 (.038)
	QDA	Baseline	.748 (.039)	.544 (.075)	.382 (.075)
		SL0	.836 (.005)	.709 (.009)	.558 (.011)
		SL	.926 (.011)	.891 (.020)	.790 (.032)
	RF	Baseline	.790 (.018)	.621 (.035)	.460 (.038)
		SL0	.820 (.005)	.685 (.008)	.532 (.009)
		SL	.929 (.009)	.899 (.018)	.803 (.027)
GLM + QDA + RF	SL0	.838 (.004)	.714 (.008)	.564 (.009)	
	SL	.945 (.005)	.927 (.009)	.844 (.017)	

Note: see Appendix A.1 of the supplementary materials for detailed simulation settings.

Table 2. Binary classification results on in vivo data. The weight for each resolution was calculated as the average from 5-fold Cross-Validation.

Base Learner	Method	Classification Results			Weight for Each Resolution		
		AUC	S80	S90	1 × 1	2 × 2	3 × 3
GLM	Baseline	0.735	0.582	0.423	—	—	—
	SL0	0.775	0.651	0.514	0.818	1.205	1.483
	SL	0.819	0.728	0.590	1.761	1.372	2.956
QDA	Baseline	0.737	0.594	0.431	—	—	—
	SL0	0.761	0.635	0.490	1.301	0.757	0.854
	SL	0.803	0.696	0.569	2.274	1.018	1.811
RF	Baseline	0.685	0.485	0.292	—	—	—
	SL0	0.738	0.563	0.408	0.780	0.637	1.029
	SL	0.836	0.738	0.587	2.866	1.540	2.694
GLM + QDA + RF	SL0	0.778	0.647	0.496	—	—	—
	SL	0.825	0.709	0.543	—	—	—

Table 3. Simulation results for classification of the ordinal clinical significance of PCa assuming strong regional heterogeneity and strong between-voxel correlation ($\sigma^2 = 10$, $\phi = 0.5$, $\nu = 1.5$) using GLM as the base learner.

Method	True Category	Classification Results			Overall Error Rate	
		Classification Table	FPR	FDR		
Baseline	1	60217	0	9822	0.14	0.38
	2	17083	0	10932	1.00	NA
	3	20475	0	21548	0.49	0.49
SL0 + W_1	1	61296	0	8763	0.13	0.34
	2	15311	0	12704	1.00	NA
	3	16359	0	25664	0.39	0.46
SL + W_1	1	64001	2598	3440	0.09	0.1
	2	13379	3804	10832	0.86	0.60
	3	4207	2837	34979	0.17	0.29
SL0 + W_2	1	48390	13488	8160	0.31	0.25
	2	7797	7943	12275	0.72	0.73
	3	8224	8515	25284	0.40	0.45
SL + W_2	1	54194	13919	1925	0.23	0.12
	2	6582	13643	7790	0.51	0.63
	3	1150	9477	31396	0.25	0.24

Note: see Appendix A.2 of the supplementary materials for detailed simulation settings.

Table 4. Ordinal classification results on in vivo data using GLM as the base learner and predicted probabilities for categories 1 and 2 as the stage-one output.

Method	True Category	Classification Results			FDR	Overall Error Rate	
		Classification Table	FPR	1	2	3	
Baseline	1	88492	0	495	0.007	0.159	0.165
	2	6151	0	92	1.000	NA	
	3	10930	0	777	0.907	0.437	
SL0 + W_1	1	87030	0	1957	0.022	0.138	0.158
	2	5953	0	290	1.000	NA	
	3	8681	0	3026	0.698	0.405	
SL + W_1	1	87022	0	1965	0.022	0.129	0.140
	2	5951	0	292	1.000	NA	
	3	6769	0	4938	0.598	0.336	
SL0 + W_2	1	65893	15149	7945	0.241	0.073	0.304
	2	2442	1840	1961	0.718	0.905	
	3	2949	2100	6658	0.432	0.575	
SL + W_2	1	63726	18912	6349	0.253	0.063	0.315
	2	2317	2618	1308	0.661	0.901	
	3	1885	2863	6959	0.401	0.519	

Table 5. Ordinal classification results on in vivo data using GLM as the base learner and predicted cancer categories as the stage-one output.

Method	True Category	Classification Results					Overall Error Rate	
		Classification Table			FPR	FDR		
		1	2	3				
Baseline	1	88492	0	495	0.006	0.162	0.165	
	2	6151	0	92	1.000	NA		
	3	10930	0	777	0.934	0.430		
SL0 + W_1		1	2	3				
	1	87850	0	1137	0.013	0.151	0.159	
	2	6083	0	160	1.000	NA		
SL + W_1	3	9583	0	2124	0.819	0.379		
		1	2	3				
	1	87865	0	1122	0.013	0.138	0.143	
SL0 + W_2	2	6173	0	70	1.000	NA		
	3	7874	0	3833	0.673	0.237		
		1	2	3				
SL + W_2	1	86039	0	2948	0.033	0.131	0.155	
	2	5524	0	719	1.000	NA		
	3	7437	0	4270	0.635	0.462		
		1	2	3				
	1	77261	8268	3458	0.132	0.081	0.206	
	2	4231	1418	594	0.773	0.887		
	3	2576	2862	6269	0.465	0.393		

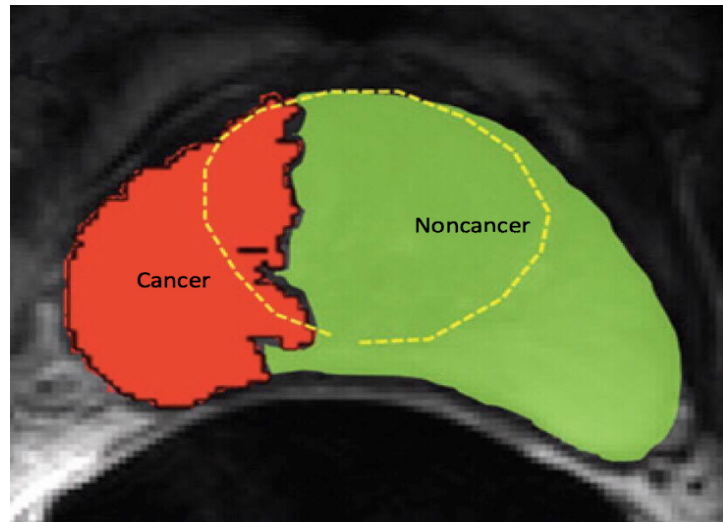


Figure 1. The annotated image of an example prostate slice. Red and green indicate annotated cancer and noncancer voxels, respectively. The yellow dashed curve divides the prostate gland into peripheral zone (PZ, the area inside the curve) and central gland (CG, the area outside the curve).

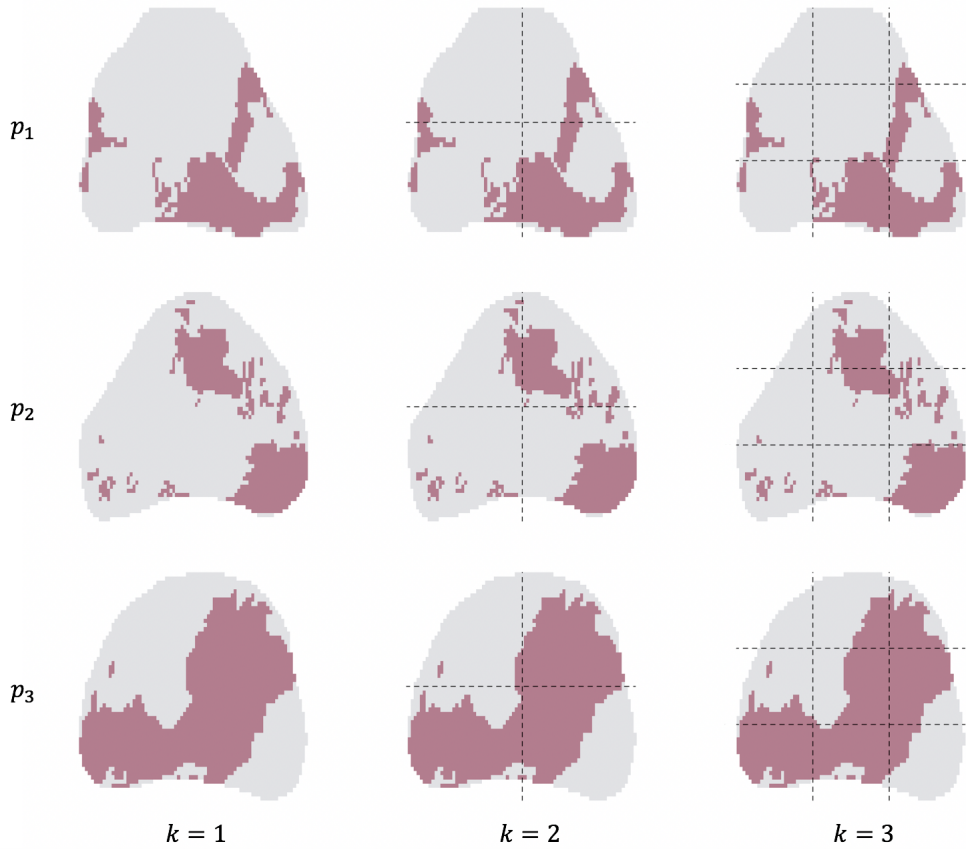


Figure 2. Region segmentation for three example prostates (p_1 , p_2 and p_3) under resolutions $k \times k$, $k \in \{1, 2, 3\}$.

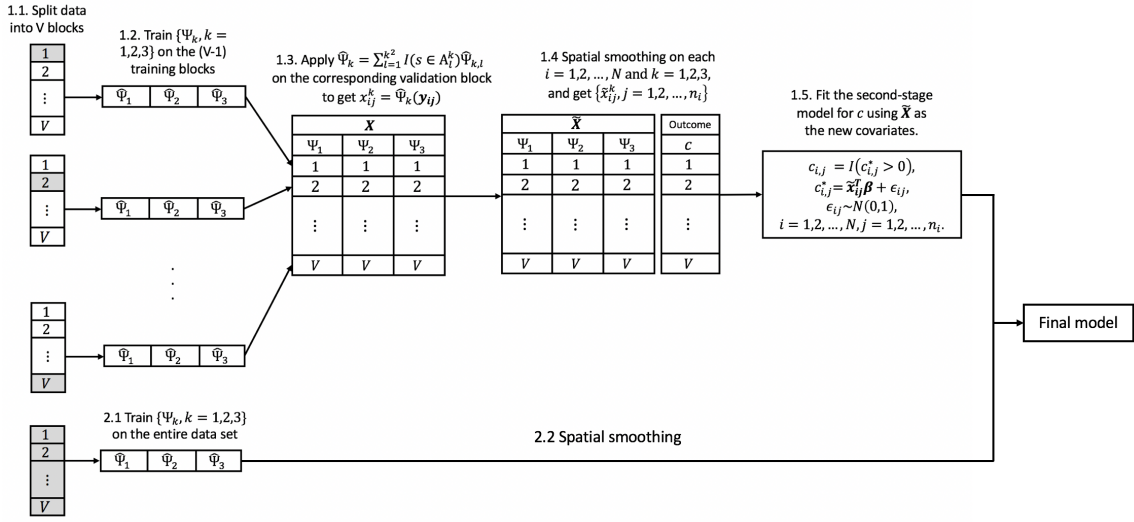


Figure 3. Flow chart of the proposed classification algorithm for voxel-wise binary PCa status. The total number of resolutions used for prostate segmentation is set to $K = 3$ for illustration.